Asian Journal of Chemistry; Vol. 36, No. 7 (2024), 1681-1692

ASIAN JOURNAL OF CHEMISTRY

https://doi.org/10.14233/ajchem.2024.31863

Development of Platinum-Free Yttrium-Ion-Substituted NiS-Graphene Nanocomposites for DSSC and Photocatalytic Applications

G. PRIYADHARSHINI[1], D. GEETHA[1,*] and P.S. RAMESH[2]

[1]Department of Physics, Annamalai University, Chidambaram-608002, India
[2]Department of Physics, Thiru Kolanjiappar Government Arts and Science College, Virudhachalam-606001, India

*Corresponding author: E-mail: geeramphyau@gmail.com

Received: 3 May 2024; *Accepted*: 17 June 2024; *Published online*: 29 June 2024; AJC-21688

A good catalytic material for the counter electrode is necessary for the dye sensitized solar cell (DSSC), which must have low cost and high power conversion efficiency. Hence, this study aims to develop an efficient graphene based yttrium doped NiS (Y-NiS/GO) nanocomposite as a counter electrode material which is an alternative material to replace platinum in DSSC. For this, NiS/GO and yttrium doped NiS/GO composite were prepared by facile hydrothermal method. The structural, size, shape and physical properties of synthesized samples were characterized by XRD, FESEM-EDX, PL, UV-DRS techniques and to evaluate the properties of the oxidation state of nanocomposite, XPS technique were adopted. The XPS confirm the elements present in sample, further, series resistance (R_s) of yttrium doped NiS/GO composite has been calculated by impedance measurement (EIS). The conversion efficiency of solar cell increases from 2.72% to 3.23%. The same material is used as a nanophoto catalytst for degrading malachite green dye under natural sunlight. The photocatalytic activities of NiS, NiS/GO and Y-NiS/GO was examined and the photodegradation increases from 86% to 97% within 180 min at pH 8.

Keywords: Yttrium, Graphene oxide, Nickel sulfide, DSSC counter electrode, Photodegradation, Malachite green.

INTRODUCTION

Continuous research and development is crucial to overcome certain obstacles and optimize the use of photovoltaic systems for entrapping the maximum energy sources [1]. The focus of these efforts is on improving solar panel efficiency and durability, reducing manufacturing costs, advancing energy storage technologies, optimizing system design and addressing environmental and social impacts linked to widespread solar energy adoption [2]. It specifically discusses the possibilities of photovoltaic systems in directly harnessing solar energy and transforming it into electrical energy [3]. While the adoption of photovoltaicsystems is increasing globally, there are still significant issues and challenges that need to be addressed to fully realize their potential in meeting global energy demands [4]. These challenges may include issues related to efficiency, cost-effectiveness, scalability, energy storage and integration into existing energy infrastructures [5].

Research is ongoing to develop materials and technologies that can enhance the efficiency of photovoltaic systems [6]. Developing new materials with optimal bandgap properties to better match the solar spectrum and maximize energy conversion [7]. Tandem or multi-junction solar cells utilize various layers of distinct materials with different band gaps, enabling them to capture a broader range of sunlight spectra. This technique can importantly increase efficiency by reducing energy losses from the unused portions of the solar spectrum. Various strategies are employed in the application of DSSC to enhance efficiency. Nickel sulfide (NiS) is a commonly used material in DSSCs due to its strength and moderate charge transport capacity. Charge recombination is a significant issue in DSSCs, as it directly impacts the device's efficiency. Similarly, surface modification can also influence the adsorption of dye molecules onto the photoanode surface [8,9].

Rare earth elements possess distinctive characteristics that make them valuable for various applications, including DSSCs, where their unique electronic configurations and intermediate energy states contribute to their versatility in functional materials [10,11]. Their substitution improves electron injection from the dye to the TiO_2 photoanode [12], while the NiS/GO counter

electrode enhances the separation of photoelectron-hole pairs, ultimately increasing cell efficiency and suggests that these materials can effectively absorb light.

Uplane *et al.* [13] developed a straight forward method for fabricating Ni/NiS electrodes by anodically oxidizing nickel in an acidic sulfide solution. However, concerns remain regarding the long-term capacity of the metallic nickel substrate in the corrosive I/I_3 electrolyte used in DSSCs. The presence of functional groups in GO nanocomposite further influences its effectiveness in photodegradation processes. However, its electrocatalytic activity for reduction of iodine is not satisfactory because of its less active site. To improve the active sites and light conversion efficiency, graphene oxide with metal sulfides were chosen [14,15]. Whereas, nickel sulfide is selected in several studies because of its low resistivity (10^{-5}–10^{-4} Ω cm) to enhance the efficiency of DSSC, conducting polymers with various carbonaceous materials [16,17]. Moreover, in their electronic configuration, a filled VB and an empty CB, makes them well-suited for catalyzing the photodegradation reactions. Nevertheless, NiS encounters a notable constraint due to its wide band gap (3.12 eV), which diminishes its performance in sunlight, affecting its photosensitivity. While there have been several research on platinum free counter electrodes, their improvement can be further enhanced by using redox active and conducting materials [18,19].

To address these issues, researchers have focused on creating hybrid structures of metal sulfides doped onto conductive graphene oxide (GO) nanostructures. This approach aims to enhance the photodegradation process by combining the properties of both rare earth metal and NiS/GO. Sulfide based semiconductor possessing broad band gap that has been mentioned as an excellent photocatalyst in visible light region. The band gap of NiS nanostructures is 2.3eV; the dye degradation efficiency depends on the adsorption property of photocatalysts and pollutant molecules. Recent studies have focused on doping with transition metals and noble metal ions, while there has been limited research on doping with rare earth ions [20,21].

The presence of GO, along with yttrium, implies potential for improved charge transfer at the cathode, thereby enhancing overall DSSC performance. Studies indicate that defects like nickel vacancies (V_{Ni}) and interstitial sulfur (V_s) affect the optical and electrical conductivity of NiS material [22,23]. While some defects exhibit localized moments, others are non-magnetic. Despite its susceptibility to oxidation when heated, yttrium remains highly stable in air. To date, there has been no prior research on yttrium doping in NiS/GO as a counter electrode for DSSCs. Consequently, we investigated the photo catalytic effects of yttrium doping on NiS/GO by degrading malachite green aqueous dye solution under natural sunlight irradiation and assessed the mechanisms underlying the photocatalytic performance of NiS/GO through rare earth ion doping, such as yttrium. The objective of this research is to assess the potential of these materials, particularly yttrium substituted NiS/GO nanocomposite, in improving the photovoltaic performance of DSSC and degradation of organic pollutants when exposed to natural sunlight conditions.

EXPERIMENTAL

The chemicals *viz*. nickel nitrate hexahydrate ($Ni(NO_3)\cdot 6H_2O$), thiourea, hydrogen peroxide, potassium permanganate, hydrochloric acid, yttrium nitrate hexahydrate ($Y(NO_3)\cdot 6H_2O$) and graphite powder used for the synthesis were procured from Sigma-Aldrich Company.

Synthesis of yttrium doped NiS/GO nanocomposite: Graphene oxide (GO) was synthesized *via* a modified Hummer's method. Initially, 5 g of graphite powder was mixed with 50 mL of H_2SO_4 and 30 mL of nitric acid and stirred for 2 h. Then, 15 g of $KMnO_4$ was mixed to the suspension over 90 min while maintaining the temperature between 0-4 ºC using an ice/water bath. After that 930 mL of H_2O was slowly added over 120 min. Finally, 50 mL of 35% H_2O_2 was introduced and the mixture was stirred and centrifuged. The resulting precipitate was washed with 0.1 M HCl followed by demineralized water and then dried in a hot air oven at 60 ºC to obtain GO.

The yttrium-doped NiS/GO composite was prepared using three different quantities of yttrium dopant, specifically 0.2, 0.4, and 0.8 g. of $Y(NO_3)\cdot 6H_2O$. The three different dopant concentrations were added into the three different conical flask of NiS/GO as prepared. The above solution stirred for 0.5 h and kept in an autoclave at 120 for 5 h. In that 0.8g of yttrium do pant was identified as a best concentration for yttrium.

Fabrication of counter electrode (CE): Fluorine doped tin oxide (FTO) sheets, measuring (1.5 cm × 1.5 cm × 0.22 cm) and with dried air resistance, were employed. A limited area on the FTO was defined using polytetrafluoroethylene (PTFE) tape, enabling film deposition and electrochemical studies on a 1 cm^2 electrode.

Fabrication of DSSC: The synthesized yttrium doped NiS/GO (Y-NiS/GO) samples were applied onto FTO glass substrates as counter electrodes, while another FTO glass substrate was coated with TiO_2 to serve as a photoanode. Afterwards, the TiO_2-coated substrate was submerged in N719 dye (ruthenium dye) for a day, enabling the dye molecules to interact with the TiO_2 photoanode under dark conditions. Once the dye molecules were absorbed by the TiO_2 photoanode, the counter electrodes and photoanodes were assembled together with an iodine electrolyte, sandwiching them. This setup enabled electron flow from the CE to the photoanode using the iodine solution under a solar simulator light to obtain an I-V characteristic curve.

Photocatalytic measurement: The photocatalytic process using yttrium-doped NiS/GO was conducted with malachite green dye (MG) at a fixed concentration of 10^{-3} M. The dye was mixed in 400 mL of deionized water, after which 100 mL of dye solution was taken and reduced to 50 mL. Then, 150 mg of yttrium-doped NiS/GO catalyst was added to initiate the photocatalytic process. Samples were collected after every 0.5 h in test tubes and the catalyst containing dye solutions in the test tubes underwent degradation. The collected samples were analyzed using UV-visible spectrometer analysis.

Characterization: The crystallite sizes of the samples prepared were examined using XRD with a D8-Advance X-ray diffractometer (Germany Bluker) at room temperature. Cu*K*α radiation (λ = 0.15406 nm) with an accelerating voltage of 40

kV and an emission current of 20 mA were utilized. The morphological characteristics of the product were evaluated through FESEM/EDX analysis using the CARL ZEISS-SIGMA model 300 instrument. The UV-vis diffuse reflectance spectra (DRS) were recorded in the wavelength range of 300-800 nm using a UV-vis spectrophotometer (Shimadzu UV-3600), with $BaSO_4$ serving as a reference. The chemical composition and oxidation state of the sample were investigated using a Thermo-Fisher instrument (XPS). Cyclic voltammeter (CV) and impedance (EIS) measurements were analyzed through an electrochemical workstation (AUTOLAB). Hall Effect was performed using a magnet kit (model # AMP55T) at various temperatures from 80 K to 350 K. The I-V characteristics were determined using a solar simulator measurement system with a Class a lamp: 300 W and a target area of 50 mm × 50 mm. The photocatalytic degradation studies were conducted using a UV-visible spectrophotometer.

RESULTS AND DISCUSSION

Thermal studies: The thermal analysis (TG-DTA) was analyzed at room temperature to identify the phase changes of the synthesized nanocomposite [24]. The mass changes have occurred when the temperature had been increased. The first weight loss of the sample was observed at 109 ºC, which shows the evaporation of water in the prepared sample. The endothermic reaction during the process shows the dehydration of the sample. The second weight loss was observed at 330 ºC as shown in Fig. 1.

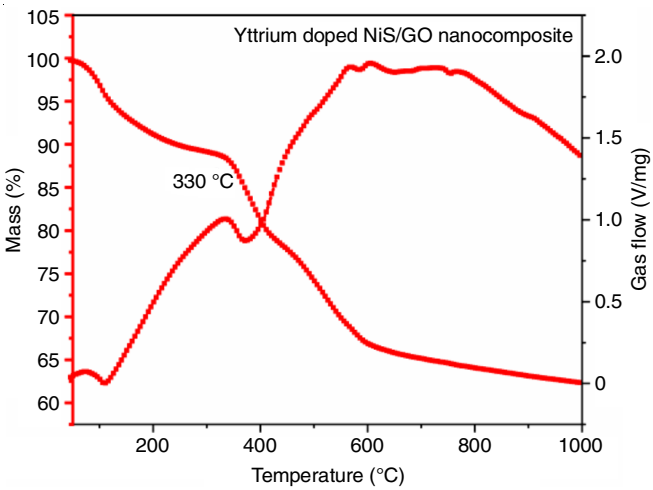

Fig. 1. TG-DTA curve of yttrium (Y^{3+}) doped NiS/GO nanocomposite

Structural studies (XRD): XRD was utilized to determine the crystalline structure of the powdered sample. Fig. 2a-d illustrates the XRD analysis of graphene oxide (GO), nickel sulfide (NiS), NiS/GO composite and yttrium-doped NiS/GO. (i) The peaks of the synthesized GO are matched with the JCPDS card no. 75-2078 and exhibited 2θ values of 11.08º, corresponding to the peak position plane (002), as shown in Fig. 2a. (ii) Pure NiS peak diffraction displayed 2θ values of 20º, 29º, 34º and 36º, 42º, 45º, 53º with a crystallite size of approximately 36 nm (Fig. 2b). (iii) For NiS/GO composite, the diffraction peaks showed the 2θ values varying between 20º, 24º, 30º, 34º, 38º, 45º, 53º with a crystallite size of about 40 nm (Fig. 2c) and (iv) yttrium doped NiS/GO material exhibited the diffraction peaks at 2θ values varying between 30º, 34º, 43º, 45º, 53º with a crystallite size of about 44 nm. The plane values for NiS, NiS/GO and yttrium-doped NiS/GO were identified as (015), (303), (306) and (330), matching the JCPDS card no. 76-2306, as depicted in Fig. 2d.

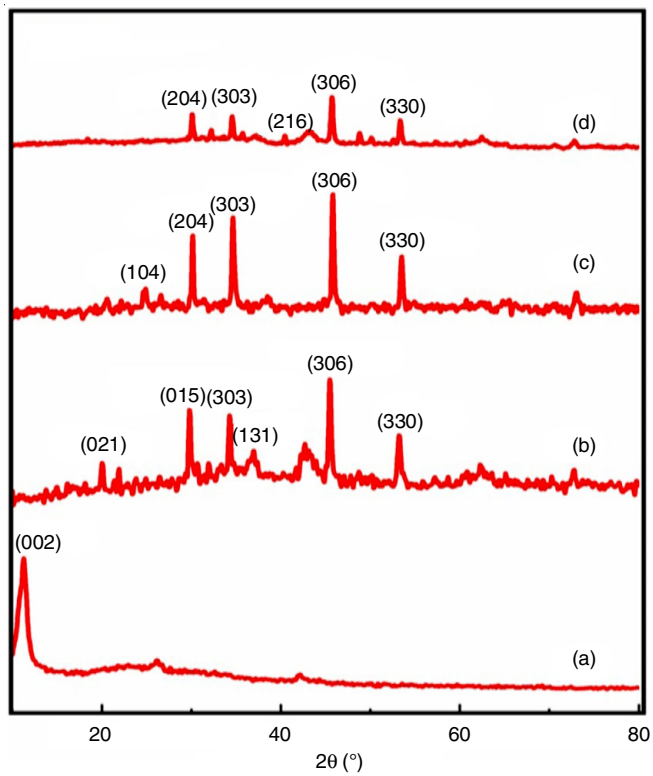

Fig. 2. X-ray diffraction analysis of (a) GO, (b) NiS, (c) NiS/GO, (d) yttrium (Y^{3+}) doped NiS/GO nanocomposite

However, an increase in doping is observed to result in a decrease in the intensity of diffraction peaks (and hence crystalline). Moreover, the size of nanoparticles, as determined by Scherrer's formula, is seen to increase with yttrium doping. These effects can be attributed to the larger ionic radii of Y^{3+} ions (0.89 Å), which either replace Ni^{2+} ions (0.74 Å) are incorporated into the NiS structure. At a doping concentration of 0.8 g wt.%, two additional small peaks at 30º and 45º emerge in the XRD spectrum, accompanied by a reduction in the average grain size. This indicates a modification in the crystal structure. It is possible that the larger size of incorporated yttrium ions creates obstacles for the movement of grain boundaries and restricts grain growth, thus change in the crystal size structure [25]. This also suggests that further yttrium doping could lead to additional disruption of hexagonal crystal structure, resulting in the formation of new phases. Therefore, 0.8 g wt.% doping concentration represents the upper limit for the extent of yttrium doping in NiS nanoparticles.

FESEM with EDX: The morphological images of NiS, NiS/GO and yttrium-doped NiS/GO were determined using a field emission scanning electron microscope. (i) Fig. 3a displays

the surface image of pure NiS, exhibiting a cornflake-like structure. (ii) Fig. 3b illustrates the surface image of NiS/GO, showing a wrinkled shape resembling a cornflake-like structure with graphene attached to its surface. (iii) Fig. 3c presents the yttrium-doped NiS/GO composite characterized by smaller size and aggregated-like structure. The incorporation of yttrium, a larger element compared to nickel, results in the reduction of distinct cornflake-like shape of the nanoparticles [26]. In Fig. 3a, it is evident that the prepared GOs display a sheet-like structure, providing a substantial surface area for surface modification with yttrium-doped NiS nanostructures. Fig. 3b illustrates that the synthesized yttrium-doped NiS nanoparticles adopt a flake-like morphology with a particle size of 28 nm. The concentration of Y^{3+} ions influences the abundance of Y-NiS nanoparticles observed on the surface of the GO nanosheet. The intensity of Y-NiS nanocomposite oxide increases, likely due to the larger crystalline size of Y-NiS nanoparticles, as evident from the XRD analysis. This characteristic is also beneficial in enhancing the efficiency of Y-NiS nanocomposite in DSSCs.

Atomic weight percentages were calculated accordingly and the EDX results for yttrium-doped NiS/GO (Y-NiS/GO) nanocomposites are shown in Fig. 3c. Analysis of the synthesized sample indicated the presence of yttrium (Y = 0.23%), nickel (Ni = 40.03%), sulfur (S = 32.35%), carbon (C = 16.70%) and oxygen (O = 10.69%), confirming the successful synthesis of the composite. Therefore, the EDX analysis confirms the presence of functional elements such as yttrium, nickel, sulfur and carbon without any impurities. Fig. 3d further confirms the mapping of the synthesized sample Y-NiS/GO, which reveals information about the areas where characteristic X-ray peaks for carbon (C), nickel (Ni), sulfur (S), oxygen (O) and yttrium (Y) are emitted. This information can be crucial for understanding the elemental distribution and composition of the Y-NiS/GO/FTO composite material. Analyzing the distribution of these elements can provide insights into the material's structure, composition and possibly its functional properties, especially if it's used in applications such as catalysis, energy storage, or electronics.

UV-DRS studies: The UV-DRS was performed on the synthesized samples in order to investigate their optical properties and the results are depicted in Fig. 4a-f. The absorption characteristics and optical bandgap energies of the samples were determined.

(i) The absorption edge was broadened and moved towards higher wavelengths with the increase of carbon material [27]. This resulted in an increase in the bandgap energy of the samples when graphene oxide (GO) was composited with pure NiS, attributed to the quantum confinement effect [28,29]. However, after yttrium doping on NiS/GO, the bandgap decreased gradually.

The bandgap energy of the samples was calculated using the Kubelka-Munk (K-M) model relation. The bandgap energy for pure NiS was approximately 2.3 eV, for NiS/GO composite it was around 2.9 eV and after yttrium doping on NiS/GO composite, the bandgap energy decreased to 2.6 eV. This indicates that reducing the bandgap energy makes the sample suitable

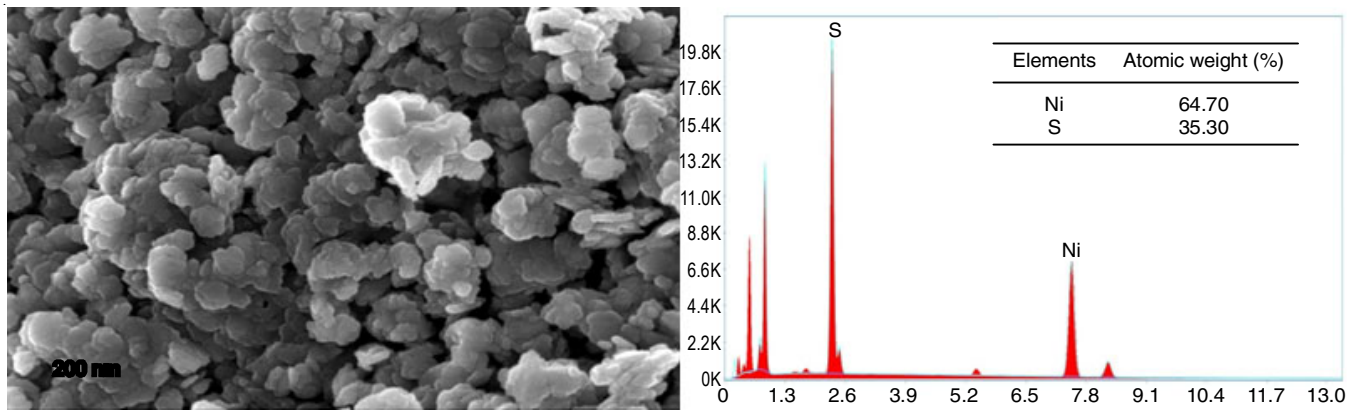

Fig. 3a. FE-SEM/EDX picture of pure NiS nanostructure

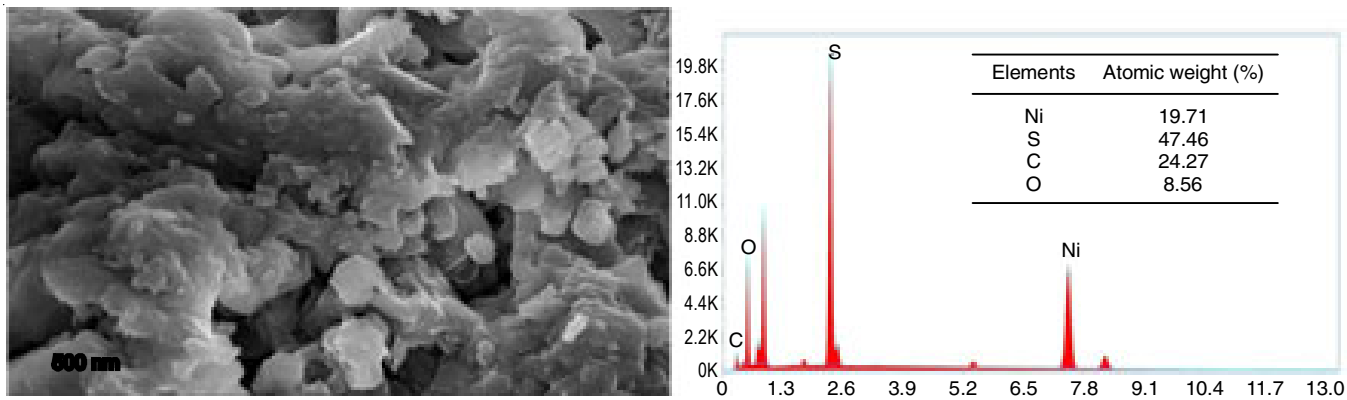

Fig. 3b. FE-SEM/EDX picture of NiS/GO nanocomposite

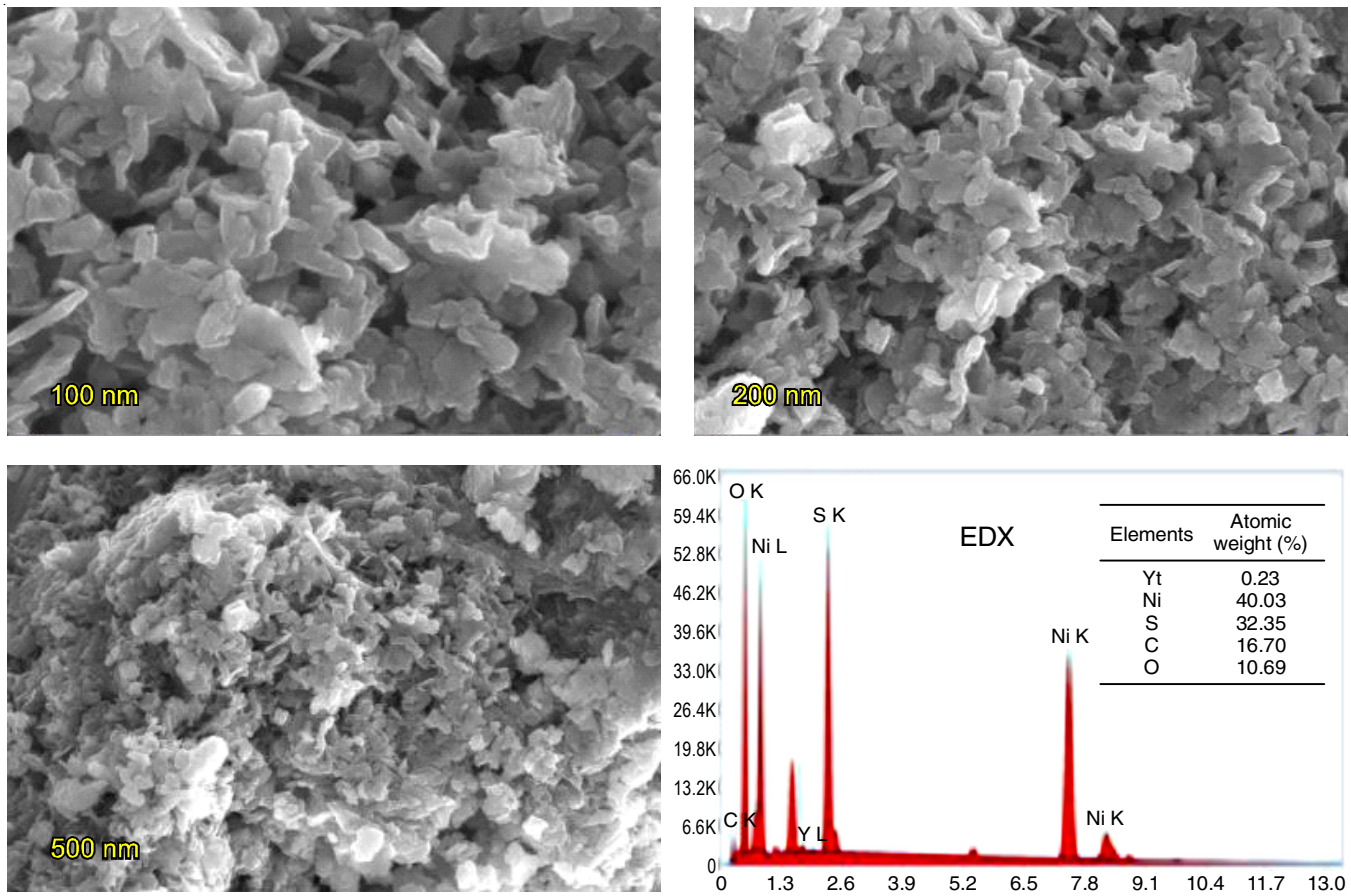

Fig. 3c. FE-SEM/EDX picture of yttrium (Y^{3+}) doped NiS/GO hybrid nanocomposite

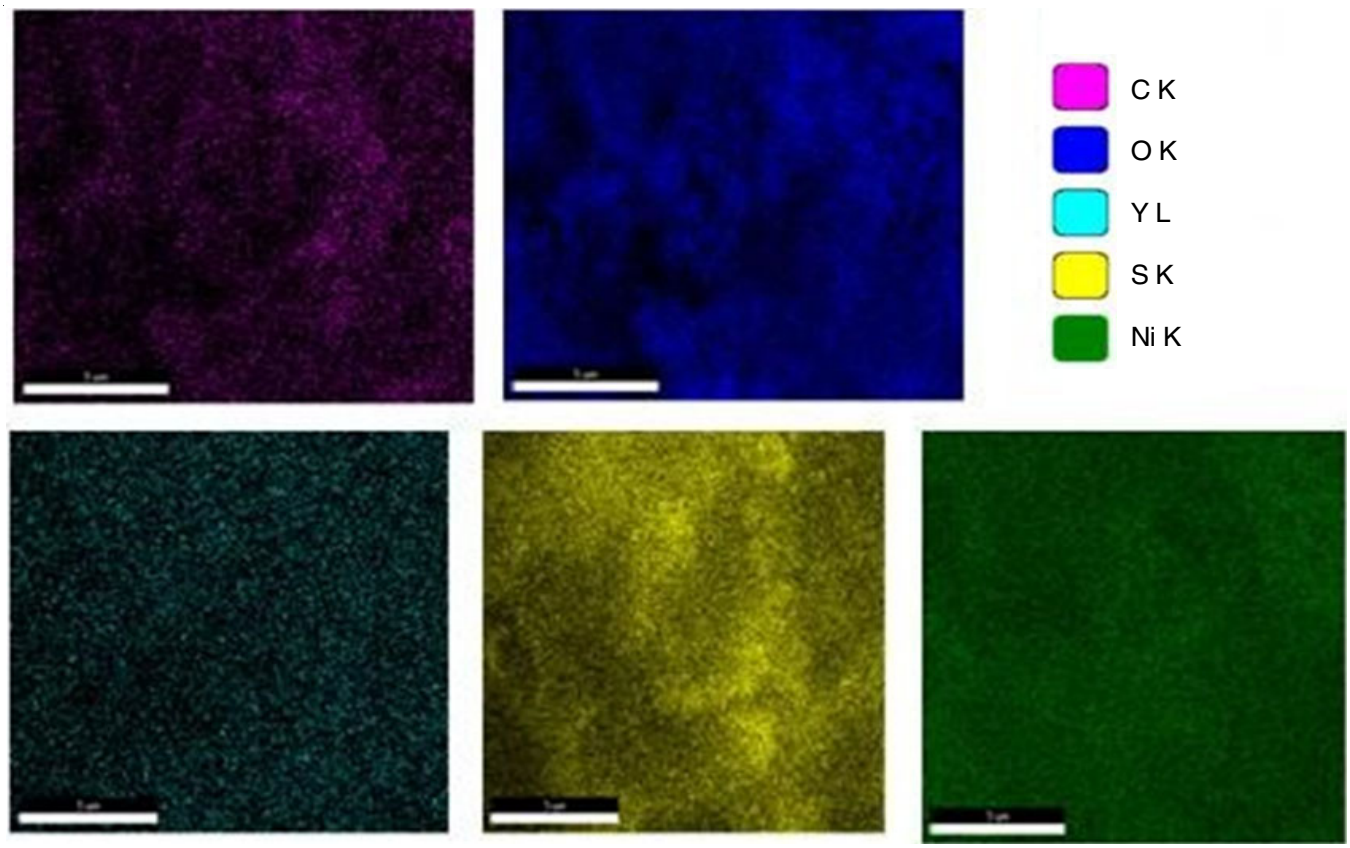

Fig. 3d. Mapping of yttrium (Y^{3+}) doped NiS/GO hybrid nanocomposite

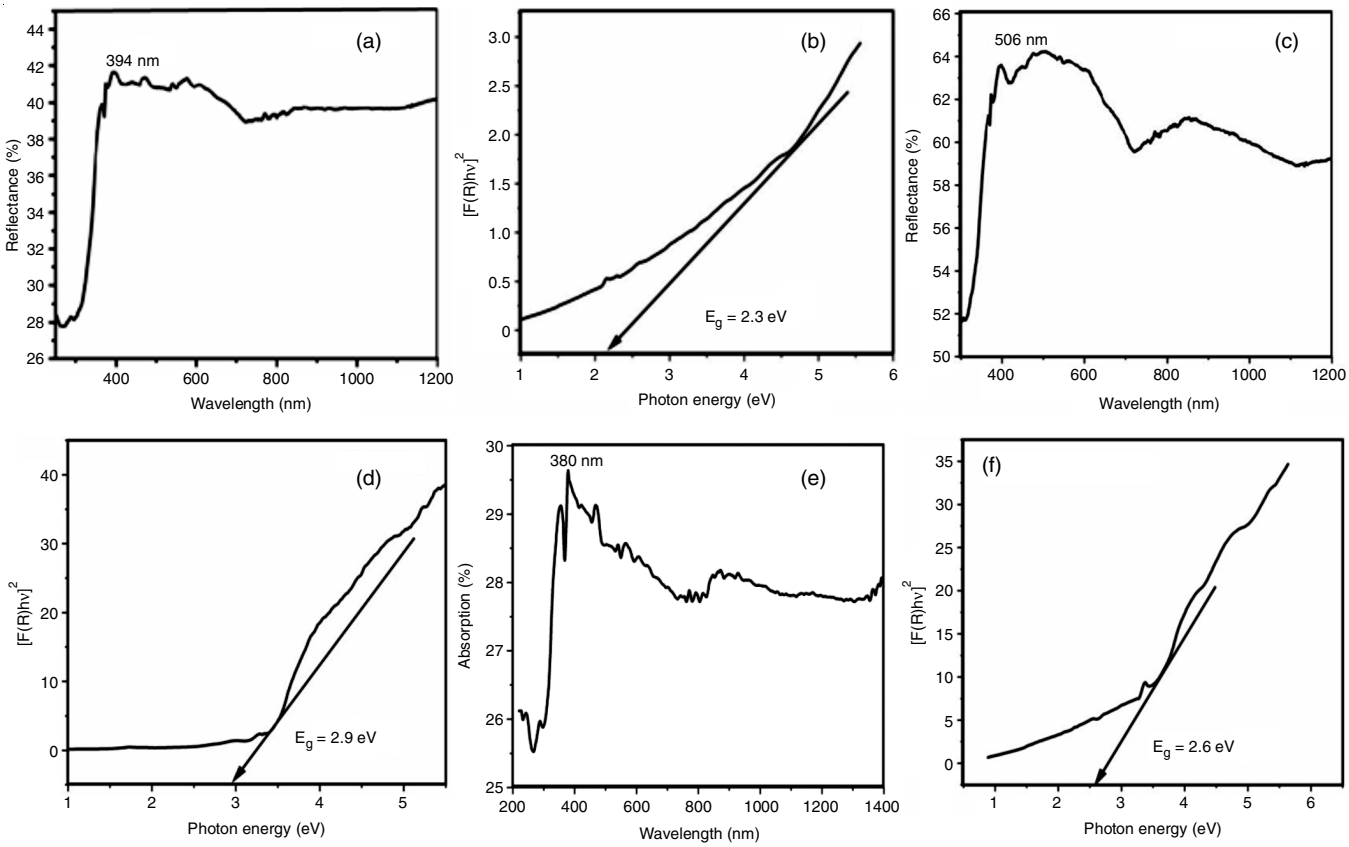

Fig. 4. (a) UV-DRS spectra of NiS, (b) Kubelka-Munk model of NiS, (c) UV-DRS spectra of NiS/GO, (d) Kubelka-Munk model of NiS/GO composite, (e) UV-DRS spectra of yttrium (Y^{3+}) doped of NiS/GO composite, (f) Kubelka-Munk model of yttrium (Y^{3+}) doped NiS/GO composite

for the photovoltaic performance. The optical bandgap of NiS/GO increased due to the decrease in particle size caused by the quantum confinement effect [30]. Furthermore, when yttrium was doped at a higher concentration of 0.9 g on NiS/GO, the energy levels of the optical bandgap decreased. This decrease in bandgap (2.6 eV) was attributed to the production of impurity atoms and the formation of vacancies between the valence band (VB) and conduction band (CB) energy levels [31]. Some reasons for the decrease in the optical bandgap include the incorporation of donor atoms such as yttrium into the conduction band of the NiS/GO lattice, the straight line bandgap of spin-orbit quantization coupling between yttrium and sulfur ions and the potential increase in the density of NiS/GO.

Photoluminescence (PL): The photoluminescent spectra of the synthesized sample Y-NiS/GO was observed at excitation wavelength corresponding to emission bands at 479 nm (Fig. 5a-c). Typically, the semiconductor nanocrystals exhibit two emission peaks: the sharp and confined exciton interstitial emission peak and the broad surface state emission peak. The yttrium doped NiS/GO composite revealed the broad and asym-

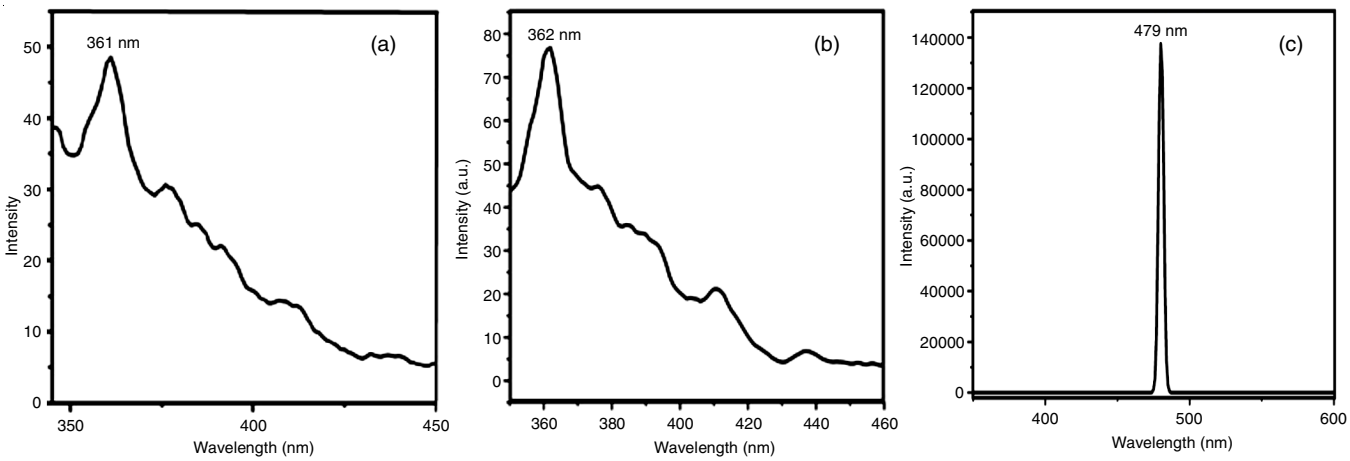

Fig. 5. Photoluminescence spectra of (a) NiS, (b) NiS/GO composite, (c) yttrium (Y^{3+}) doped NiS/GO nanocomposite

metric spectra [32]. Peaks around 479 nm were attributed to the 5*d* and 4*f* orbital transitions of Y^{3+} ions. As the concentration of yttrium increased the peak values, shifting them to higher wavelength. Remarkably, after doping yttrium onto the NiS/GO host lattice, the photoluminescence intensity slightly increases due to the higher doping concentration. Yttrium doping led to a decrease in the emission intensity of NiS while enhancing the green emission of yttrium-doped NiS/GO, which was efficient for optical properties [33]. This phenomenon suggests that an increase in yttrium concentration allows unwanted electron flow into the NiS/GO composite, potentially affecting recombination control of holes and electrons, leading to impaired photoluminescent illumination. The increase in near-band emission was attributed to straightforward recombination of positive and negative ions.

This study revealed some new luminescent phenomena in the photoluminescent spectra of Y-NiS/GO composite. The bandgap recombination of Y-NiS/GO exhibited a broadened peak around 479 nm, while the peak at 479 nm indicated some surface defects of the nanoparticles due to bounded excitation luminescence [34]. Decrease in emission peaks could affect the suppression of recombination of light-formed carriers and lead to longer charge carrier lifespans. Structural defects such as vacancies of nickel, oxygen, carbon, sulfur, nitrogen and yttrium indicate the presence of metal sulfide materials, contributing to photoluminescent spectra in the visible light region.

XPS analysis: The XPS technique was utilized to investigate the chemical composition and oxidation states of the synthesized nanoparticles [35]. The Y-NiS/GO nanocomposite exhibited elements such as yttrium (Y), nickel (Ni), sulfur (S), carbon (C) and oxygen (O), indicating the synthesis of yttrium-doped NiS/GO. In the Y-NiS/GO, the binding energies for yttrium (Y 3*d*), nickel (Ni 2*p*), sulfur (S 2*p*), carbon (C 1*s*) and oxygen (O 1*s*) peaks were recorded at 160.21 eV, 854.87 eV, 532.45 eV, 285.85 eV and 162.04 eV, respectively.

Upon observation, it was observed that the peak position of sulfur (S 1*s*) core level shifted to a higher energy level compared to pure NiS, NiS/GO composite and Y-NiS/GO [36]. Based on Paul's exclusion principle, the electronegativity value of NiS was determined to be 1.91, while for yttrium it was approximately 1.22. This suggests that electrons can potentially move from yttrium to nickel sulfide. This electron transfer results in a higher negative charge of nickel sulfide and reduces the electron binding energy of nickel and sulfide peaks. With yttrium doping on NiS/GO, the significant peak of yttrium at 285.85 eV indicates that yttrium is more relevantly a trivalent atom (Fig. 6).

Electrochemical analysis

Counter electrodes performance: Fig. 7a-d illustrates the chronoamperogram depicting the deposition process of Y-NiS/GO onto the FTO substrate. Graphene oxide, carrying negative charges, can act as doping agents. The I-V curve demonstrates the electrochemical deposition of NiS nanoparticles onto Y-NiS/GO/FTO. The high concentration of nickel ions on the surface of the counter electrode is responsible for the current density in the cathodic surface, while the anodic current density is increased by the dissolving of newly deposited nickel nanoparticles onto the Y-NiS/GO/FTO.

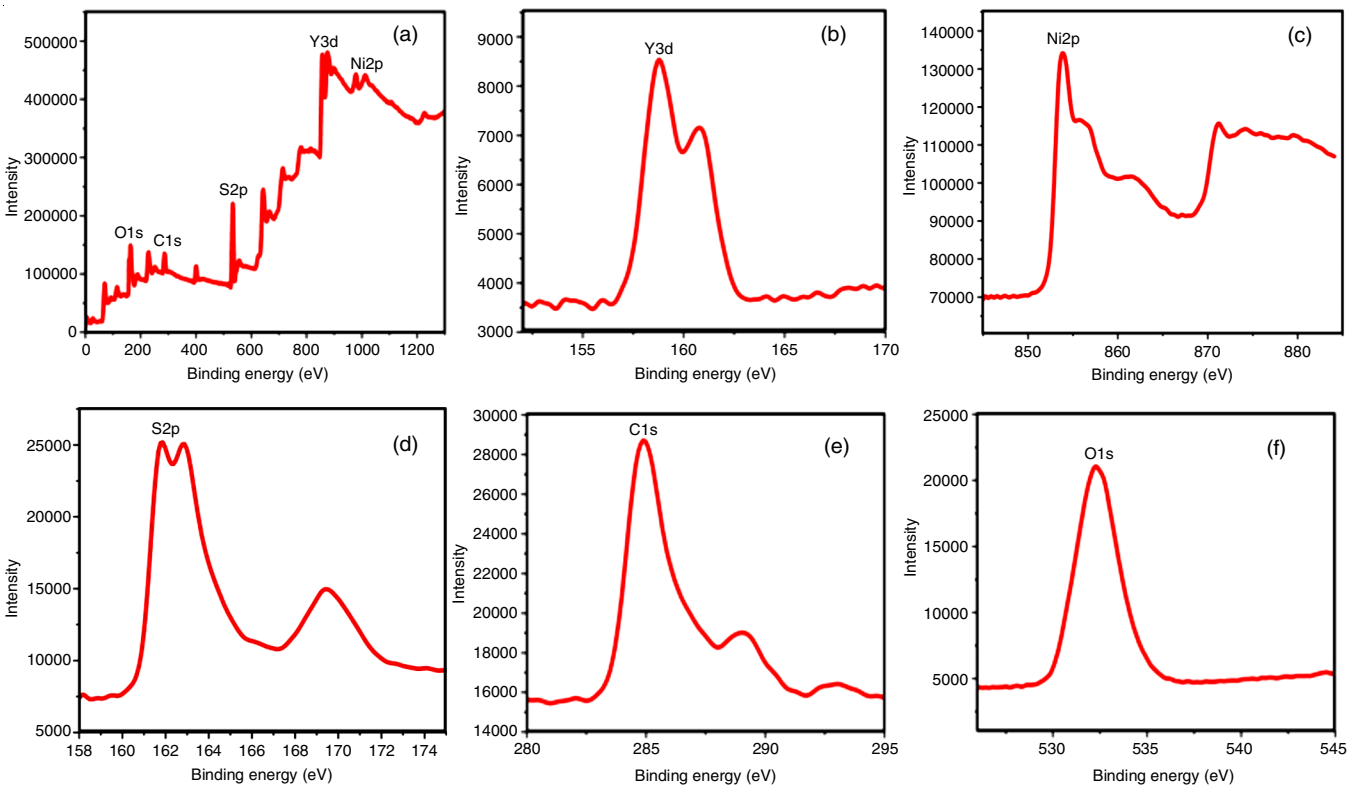

Fig. 6. XPS spectra of yttrium (Y^{3+}) doped NiS/GO composite (a) survey, (b) Y3d, (c) Ni2p, (d) S2p, (e) C1s, (f) O1s

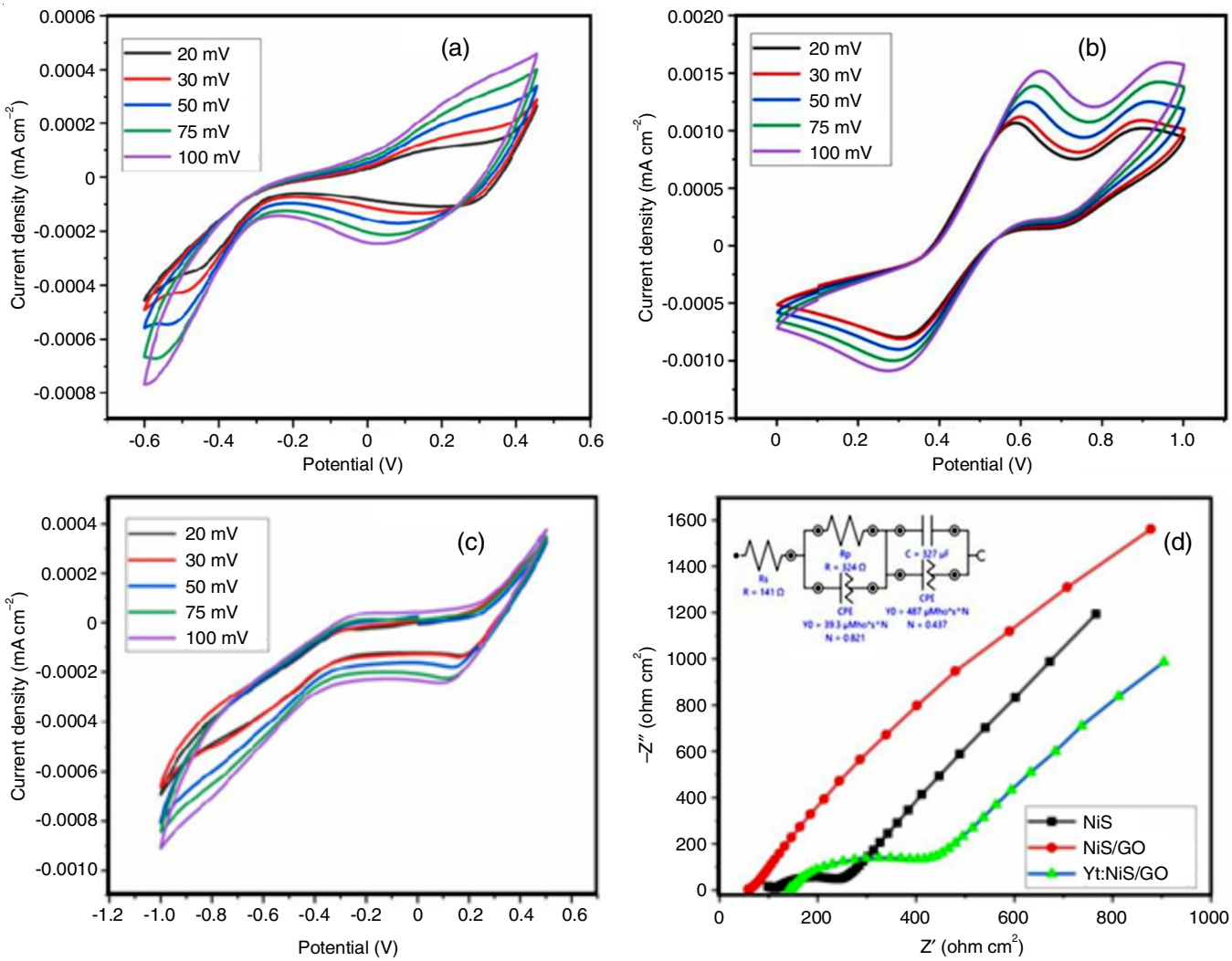

Fig. 7. CV curve of different scan rate of (a) NiS, (b) NiS/GO composite, (c) yttrium (Y^{3+}) doped NiS/GO composite; (d) electrochemical impedance spectra (EIS) of NiS, NiS/GO, yttrium doped NiS/GO

A three-electrode setup was employed, including a platinum (Pt) working electrode, a silver chloride (AgCl) reference electrode and yttrium-doped NiS/GO counter electrodes. The electrolyte solution employed contained KI salt and I_2 dissolved in acetonitrile solvent. A concentration of 0.1 g of KI was selected, likely to mitigate issues related to salt precipitation [37]. This concentration remains constant throughout the experiment. A fixed concentration of 50 mM iodine was used in electrolyte solutions. This setup suggests an experimental procedure for investigating the electrochemical properties of NiS and NiS/GO under different concentrations of iodine species. The use of acetonitrile as solvent and iodine concentrations indicates the importance of controlling experimental conditions to ensure reliable results [38].

According to the EIS data, the NiS/GO hybrid exhibits enhanced the catalytic activity due to its combination of 2D/3D electronically allowing channels provided by graphene and the unique rod-on-sheet structure of the hybrid [39]. The enhanced catalyst activity for the I^-/I_3^- redox reaction, accelerated the reaction rate, reduced diffusion resistance of I^-/I_3^- in the electrolyte and decreased electron transfer resistance at the iodine electrolyte/counter electrode (CE) interface can be attributed to the 2D/3D architecture of the catalyst. In catalytic contexts, the term "2D/3D architecture" typically denotes a blend of 2D materials, such as graphene or graphene derivatives and 3D structures, such as porous materials or nanoparticles [40]. The 2D materials provide a large surface area and excellent conductivity, facilitating efficient charge transfer and enhancing the catalytic activity. They also offer a high density of active sites for the redox reaction to occur. On the other hand, the 3D structures provide structural stability and can enhance mass transport properties. They can create pathways for the efficient diffusion of reactants and products, reducing the diffusion resistance and promoting faster reaction rates. This leads to faster reaction rates, diffusion resistance of redox species in the iodine electrolyte and reduced electron transfer resistance at the iodine electrolyte/counter electrode (CE) interface.

The performance of counter electrodes (CEs) was assessed using EIS technique. To accomplish this, two identical CE electrodes were constructed. The iodine electrolyte was then injected between the two FTO electrodes. Nyquist plots of the symmetric Y-NiS/GO cells are shown in Fig. 7d. Two semi-

circles are visible: the semicircle at high frequencies indicates the presence of resistance in the charge transfer (R_{ct}) process at the electrode/electrolyte interface, which defines the electrocatalytic performance of CEs. Conversely, GO improves the material's conductivity and assists in the formation of active sites for the I_3^-/I^- redox reaction.

The study indicates that the NiS/GO hybrid shows lower series resistance (R_s) of 59 Ω compared to the Y-NiS/GO series resistance (R_s) of 141 Ω, indicating more facile electron transfer kinetics and reduced charge recombination [41]. However, excessive doping can lead to increase R_s, possibly due to inhibited charge transfer processes, such that Y-NiS/GO has a charge transport resistance (R_{ct}) of about 324 Ω. The series resistance initially decreases and then increases with doping, consistent with the variation trends of short-circuit density (J_{sc}) and perovskite solar cells (PSC). Excessive yttrium doping can lead to compromized interconnection of NiS network, hindering the electron transfer and increasing charge recombination [42].

Cyclic voltammetry analysis shows better electrochemical behaviour for Y-NiS/GO compared to pure NiS and NiS/GO composite indicating the improved electron transfer reactions. This improvement could be attributed to the presence of Y-NiS/GO. In summary, the study highlights the importance of EIS and CV techniques in understanding the electrochemical properties and catalytic activity of DSSCs particularly in the context of composite materials like NiS/GO and the effects of yttrium doping on their performance.

Cell performance: The study explores the photovoltaic characteristics of prepared nanocomposites through the I-V characterization [43]. These nanocomposites serve as counter electrodes in DSSCs, employing N719 ruthenium dye as a sensitizer. The DSSC's effective area is 0.2 cm^2 and the performance assessment of the DSSC includes parameters such as J_{sc}, V_{oc}, FF and energy conversion efficiency (η), calculated using eqns. 1 and 2. Eqn. 1 computes the fill factor (FF) using maximum output values of current (I_{max}) and voltage (V_{max}), along with short-circuit current (I_{sc}) and open-circuit voltage (V_{oc}). Eqn. 2 determines the energy conversion efficiency (η), incorporating J_{sc}, V_{oc}, FF and input power (P_{in}) [44]. Dye sensitizer (N719) was also evaluated under an irradiance of 100 W/cm^2.

$$FF = \frac{I_{max} \times V_{max}}{I_{sc} \times V_{oc}} \quad (1)$$

$$\eta = \frac{J_{sc} V_{oc} FF}{P_{in}} \times 100 \quad (2)$$

Graphene oxide, a two-dimensional (2D) carbonaceous material, exhibits superior electrical conductivity and stability compared to pure nickel sulfide (NiS) [45]. To further improve the electrical conductivity, stability and efficiency of DSSCs, a novel counter electrode (yttrium-doped NiS/GO) was synthesized, offering ease of fabrication at a reduced cost. With a doping of 0.3 g of yttrium, the efficiency increased from 2.72% to 3.23%. The photovoltaic response parameters such as open-circuit voltage (V_{OC}), short-circuit current density (J_{sc}), fill factor (FF) and power conversion efficiency (PCE %) were calculated and summarized in both the Fig. 8 and Table-1. The larger ionic radius of yttrium (0.89 nm) compared to nickel (0.069 nm) contributed to the efficiency increase from 2.72% to 3.23%. The study illustrates the efficiency enhancement for Y-NiS/GO and NiS/GO counter electrodes in DSSCs [46]. The enhanced absorption of N719 dye (ruthenium dye) on TiO_2 in conjunction with the Y-NiS/GO counter electrode is responsible for the enhancement of all I-V parameters.

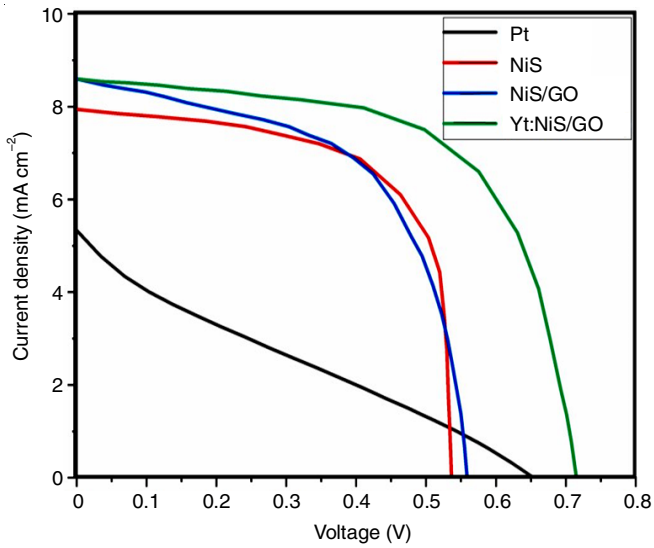

Fig. 8. Photovoltaic performance of platinum, pure NiS, NiS/GO composite, yttrium doped NiS/GO composite

Hall effect: The carrier density, Hall mobility and resistivity of NiS, NiS/GO and yttrium-doped NiS/GO composite were measured using a four-probe van der Pauw augmented Hall apparatus on an ITO glass substrate with a thickness of approximately 1 μm. The electrical properties of thin films, specifically NiS, NiS/GO (nickel sulfide/graphene oxide) and Y-NiS/GO thin films. In this experiment, all the samples exhibited p-type charge carrier conduction, which means they carried the positive charges. The p-type conductivity is characteristic of materials where positive charge carriers (holes) dominate the electrical conduction [47]. It was observed that the carrier concentration for all three samples increased (NiS > NiS/GO > Y-NiS/GO), while the resistivity decreased, indicating a better choice for photovoltaic properties. The decrease in resistivity

TABLE-1
I-V CHARACTERISTICS OF DIFFERENT COUNTER ELECTRODES

Parameters	Platinum (Pt)	NiS	NiS/GO	Yttrium doped NiS/GO
Short circuit current density, J_{sc} (mA/cm^2)	0.2867	0.5364	0.5586	0.7152
Open circuitvoltage, V_{oc} (mV)	6.6945	7.9426	8.3934	8.5901
Fill factor (FF)	34	63	59	53
Efficiency, η (%)	2.59%	2.64%	2.72%	3.23%

automatically creates oxygen vacancies, leading to an increase in the carrier mobility of the samples [48]. All three samples exhibited positive-type (p-type) current charge carrier conductivity. The carrier density, Hall resistivity and mobility were plotted against the samples and are shown in Fig. 9a-b. The increase in conductivity values (Table-2) suggests that all three samples are suitable for energy harvesting devices.

TABLE-2
HALL EFFECT PARAMETERS OF
VARIOUS COUNTER ELECTRODES

Parameters	NiS	NiS/GO	Yttrium doped NiS/GO
Carrier density	1.89	1.23	2.08
Hall resistivity	1.46	1.60	1.43
Hall mobility	2.28	4.60	4.66

Fig. 9 illustrates the correlation between the resistivity and the carrier concentrations for three samples. The highest resistivity was observed in the NiS, NiS/GO and Y-NiS/GO samples. The introduction of Ni substitutions in the (001) layer resulted in partial disorder, leading to increased carrier scattering and consequently reducing mobility. Additionally, the phase transformation from kesterite to stannite impacted the electrical properties. The XRD analysis also verifies the existence of secondary phases, which subsequently impact the electrical impedance of the samples.

Photocatalytic studies: The acceleration of the reaction process signifies the photocatalytic mechanisms. When a semiconductor material reacts with specific wavelengths of light, it initiates oxidation processes, leading to the photo catalytic degradation of pollutants [49]. The two main factors responsible for the photocatalytic dye degradation process under solar illumination are the response to sunlight and the creation of photo-induced electron-hole pairs. The possible photocatalytic mechanism occurs on the surface of Y-NiS/GO, used as a catalyst for malachite green (MG) dye [50]. When sunlight photons are absorbed by the catalyst (Y- NiS/GO), the photo-induced electrons move from the valence band (VB) to the conduction band (CB) with an energy band gap of 2.1 eV. Subsequently, the electrons react with atmospheric oxygen (O_2) and water (H_2O) to form hydrogen peroxide (H_2O_2) [51].

$$O_2^- + H_2O \rightarrow H_2O_2 \quad (3)$$

Then, the generated hydrogen peroxide (H_2O_2) reacts and combines with the electrons photocatalyst surface to produce hydroxide (OH) molecules.

$$O_2 + H_2O \rightarrow H_2O_2 \rightarrow OH \quad (4)$$

In this study, the photocatalytic process for the degradation of malachite dye using the synthesized catalyst was analyzed under natural sunlight over a period of 180 min. After the addition of catalyst, the absorption peaks began to disappear and samples were collected and analyzed for UV analysis after every 30 min. The yttrium-doped NiS/GO sample effectively degraded the malachite green dye by 97%, compared to 94% for pure NiS and 86% for the NiS/GO composite, respectively. Among the pure NiS, NiS/GO and Y-NiS/GO, good visible photons of light were observed for the photocatalytic process (Fig. 10). Hence, the nanocomposite exhibited good photocatalytic activity.

The ionic radius of Y^{3+} is 0.088 nm, which is larger than that of Ni^{2+} (0.068 nm), posing a challenge for Y^{3+} to integrate into the NiS lattice. It has been documented that rare earth salts undergo a transformation into rare earth oxides during the temperature changing calcinations process. These oxides can be evenly absorbed onto the surface of NiS, helping in the separation of charge carriers, thus their lifetimes and impeding the recombination of electron-hole pairs. As a result, Ni^{2+} can replace Y^{3+} in the lattice of rare earth oxides, forming tetrahedral Ni sites due to the significant difference in ionic radii between Ni^{2+} and Y^{3+}. This substitution creates a charge imbalance, leading to increased adsorption of $^{\bullet}OH$ ions onto the NiS catalyst surface for charge balance [52]. These surface $^{\bullet}OH$ ions can trap holes generated by sunlight irradiation, generating $^{\bullet}OH$ radicals. This process not only suppresses the recombination of photogenerated electron-hole pairs but also oxidizes and absorbs more reaction substrates, thereby effectively enhancing photocatalytic performance. Moreover, the transition of 4*f*-electrons of rare earth ions enhances the optical absorption

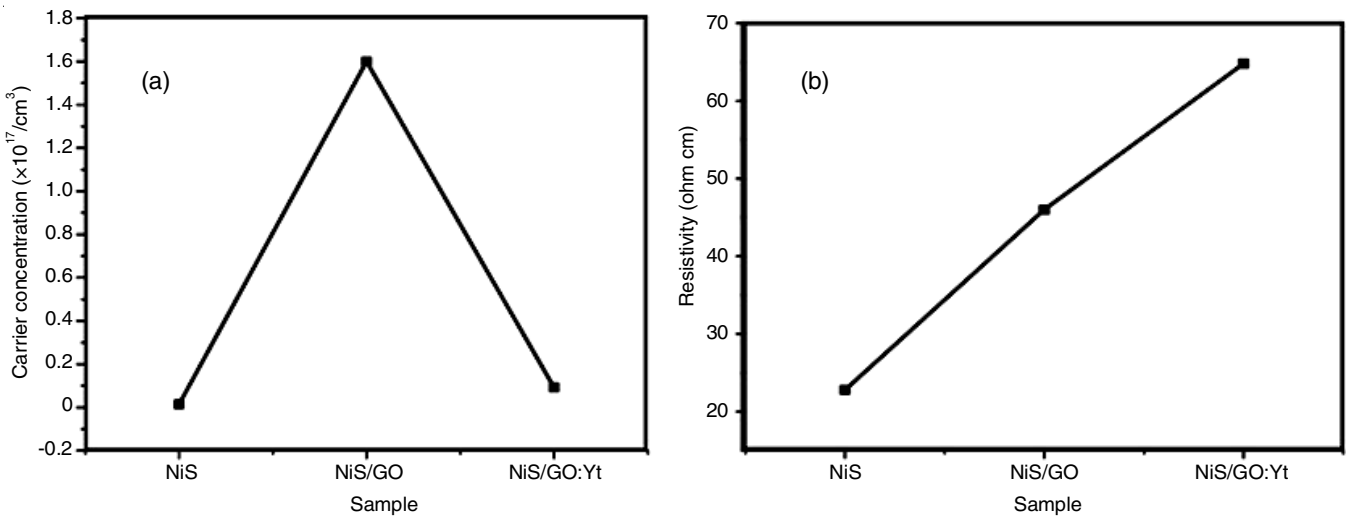

Fig. 9. (a) Carrier concentration; (b) Hall resistivity of Y-NiS/GO from Hall effect

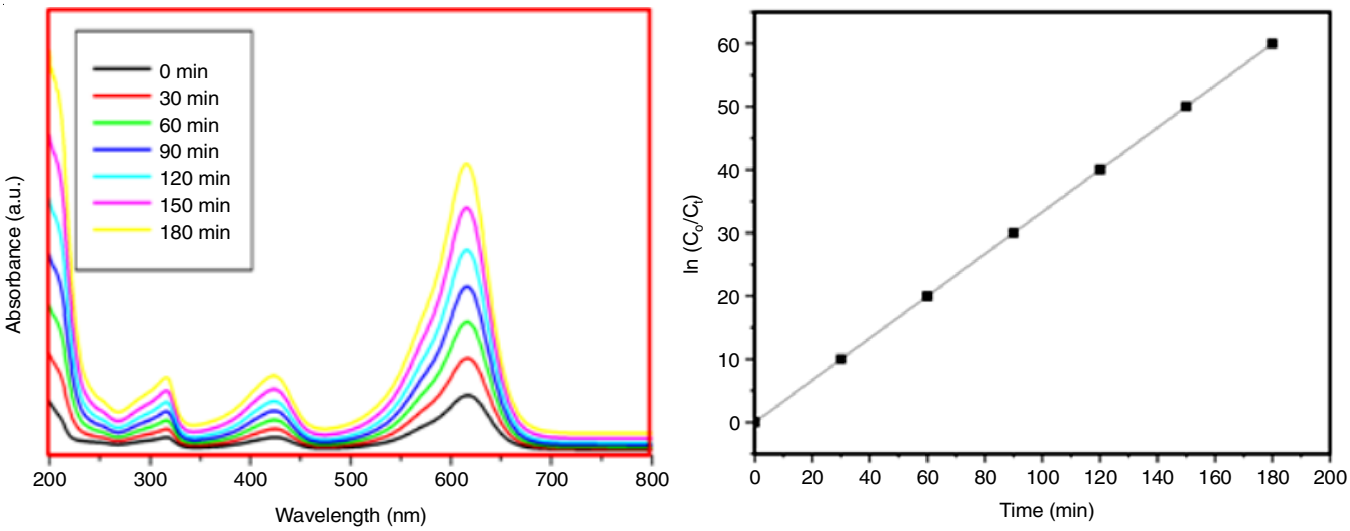

Fig. 10. UV-visible spectra, kinetic analysis and degradation efficiency of yttrium (Y^{3+}) doped NiS/GO composite

capability of NiS. In order to improve the photocatalytic performance under sunlight, doping lanthanide ions causes the optical absorption of NiS edge to shift red, which extends the photo-response range.

Conclusion

In summary, incorporation of modified GO and NiS amplified the efficiency of yttrium-doped NiS/GO as Pt-free counter electrode material for DSSCs. The yttrium-doped NiS/GO nanocomposites were successfully synthesized using a simple hydrothermal method. The incorporation of yttrium doping in the NiS/GO composite successfully adjusts the bandgap (from 2.9 to 2.6 eV) without causing significant alterations to its crystal structure. Initially, the introduction of yttrium atoms into the NiS structure begins with filling up Ni vacancies, leading to a decrease in the emission of lower doping levels. However, at increasing doping levels, the yttrium ions start occupying interstitial sites, which in turn promotes defect emission from the NiS structure, as confirmed by photoluminescence spectra. The synthesis of pure NiS, incorporation of GO into NiS as a composite and the chemical valence states of yttrium-doped NiS/GO were confirmed through XRD and XPS analysis. The method outlined for preparing Y-doped NiS/GO holds significant promise for creating intriguing hybrids aimed at fabricating high-performance Pt-free DSSCs. The FE-SEM images with EDX analysis revealed a cornflake-like shape with wrinkled morphology and uniform distribution of yttrium on NiS/GO. This study demonstrates that yttrium was successfully doped onto the NiS/GO composite and utilized as a counter electrode in DSSCs. As compared to the NiS/GO and yttrium-doped NiS/GO nanocomposite, yttrium-doped NiS/GO (Y-NiS/GO) exhibited the highest power conversion efficiency. Yttrium doped NiS/GO exhibits the PCE increased from 2.72% to 3.23%, indicating that yttrium enhances the efficiency of the solar cell and could potentially replace the expensive metal platinum counter electrode in DSSCs. Yttrium also enhanced the surface area and lattice structure of the NiS/GO composite. The synthesized Y-NiS/GO nanocomposite exhibited high charge separation and a large surface area, leading to better photocatalytic activity compared to pure NiS and the NiS/GO composite. Additionally, the degradation efficiency gradually increased with the addition of yttrium (97%) compared to pure NiS (94%) and the NiS/GO composite (86%) in terms of photocatalytic activity. Electrochemical investigations revealed that the nanostructured Y-doped NiS/GO exhibited superior electrocatalytic performance compared to NiS and NiS/GO in the I_3^-/I^- electrolyte. The concurrent presence of GO nanosheets and NiS nanoparticles in the nano-hybrid enhances film conductivity and reduces R_{ct}. The Y-doped NiS/GO catalyst accelerates the rate of the I_3^-/I^- redox reaction, leading to improved DSSC PCE compared to NiS and Y-doped NiS/GO counter electrodes.

ACKNOWLEDGEMENTS

This work was accomplished with the help of Centralised Instrumentation and Service Laboratory (CISL), Annamalai University, Alagappa University, Nanotechnology Research Center of SRM University; Bishop Heber College and DST-FIST sponsored cyclic voltammeter results from Department of Physics, Annamalai University.

CONFLICT OF INTEREST

The authors declare that there is no conflict of interests regarding the publication of this article.

REFERENCES

1. B. Munisha, B. Mishra and J. Nanda, *J. Rare Earths*, **41**, 19 (2023); https://doi.org/10.1016/j.jre.2022.03.017
2. K.V. Chandekar, M. Shkir, A. Khan, M.A. Sayed, N. Alotaibi, T. Alshahrani, H. Algarni and S. AlFaify, *J. Mater. Res. Technol.*, **15**, 2584 (2021); https://doi.org/10.1016/j.jmrt.2021.09.072
3. K. Saranya and L. Kavitha, *Mater. Today Proc.*, **51**, 1743 (2022); https://doi.org/10.1016/j.matpr.2020.11.910
4. J. Shen, R. Cheng, Y. Luo, Y. Chen, X. Chen, Z. Sun and S. Huang, *J. Solid State Electrochem.*, **19**, 1045 (2015); https://doi.org/10.1007/s10008-014-2704-8
5. T. Shanmugapriya and J. Balavijayalakshmi, *Asia-Pac. J. Chem. Eng.*, **16**, e2598 (2021); https://doi.org/10.1002/apj.2598

6. S. Li, R. Ma, X. Zhang, X. Li, W. Zhao and H. Zhu, *Mater. Des.*, **118**, 163 (2017); https://doi.org/10.1016/j.matdes.2017.01.037
7. S.P. Bremner, C. Yi, I. Almansouri, A. Ho-Baillie and M.A. Green, *Solar Energy*, **135**, 750 (2016); https://doi.org/10.1016/j.solener.2016.06.042
8. J.A. Castillo-Robles, E. Rocha-Rangel, J.A. Ramírez-de-León, F.C. Caballero-Rico and E.N. Armendáriz-Mireles, *J. Compos. Sci.*, **5**, 288 (2021); https://doi.org/10.3390/jcs5110288
9. K. Sharma, V. Sharma and S.S. Sharma, *Nanoscale Res. Lett.*, **13**, 381 (2018); https://doi.org/10.1186/s11671-018-2760-6
10. N. Yao, J. Huang, K. Fu, X. Deng, M. Ding and X. Xu, *RSC Adv.*, **6**, 17546 (2016); https://doi.org/10.1039/C5RA27033B
11. H. Lian, Z. Hou, M. Shang, D. Geng, Y. Zhang and J. Lin, *Energy*, **57**, 270 (2013); https://doi.org/10.1016/j.energy.2013.05.019
12. L.P. D'Souza, R. Shwetharani, V. Amoli, C.A.N. Fernando, A.K. Sinha and R.G. Balakrishna, *Mater. Design*, **104**, 346 (2016); https://doi.org/10.1016/j.matdes.2016.05.007
13. M.M. Uplane, S.H. Mujawar, A.I. Inamdar, P.S. Shinde, A.C. Sonavane and P.S. Patil, *Appl. Surf. Sci.*, **253**, 9365 (2007); https://doi.org/10.1016/j.apsusc.2007.05.069
14. S. Li, R. Ma, X. Zhang, X. Li, W. Zhao and H. Zhu, *Mater. Des.*, **118**, 163 (2017); https://doi.org/10.1016/j.matdes.2017.01.037
15. R. Viswanath, H.S.B. Naik, Y.K.G. Somalanaik, P.K.P. Neelanjeneallu, K.N. Harish and M.C. Prabhakara, *J. Nanotechnol.*, **2014**, 924797 (2014); https://doi.org/10.1155/2014/924797
16. N.I. Akpu, A.D. Asiegbu, L.A. Nnanna, I.L. Ikhioya and T.I. Mgbeojedo, *Arab. J. Sci. Eng.*, **47**, 7639 (2022); https://doi.org/10.1007/s13369-021-06455-0
17. S. Sharma, I. Singh, Natasha and A. Kapoor, *Mater. Sci. Semicond. Process.*, **56**, 174 (2016); https://doi.org/10.1016/j.mssp.2016.08.008
18. P. Qin, A.L. Domanski, A.K. Chandiran, R. Berger, H.J. Butt, M.I. Dar, T. Moehl, N. Tetreault, P. Gao, S. Ahmad, M.K. Nazeeruddin and M. Grätzel, *Nanoscale*, **6**, 1508 (2014); https://doi.org/10.1039/C3NR05884K
19. W. Wang, Y. Liu, J. Sun and L. Gao, *J. Alloys Compd.*, **659**, 15 (2016); https://doi.org/10.1016/j.jallcom.2015.10.254
20. X. Niu, S. Li, H. Chu and J. Zhou, *J. Rare Earths*, **29**, 225 (2011); https://doi.org/10.1016/S1002-0721(10)60435-8
21. W. Zhang, K. Wang, S. Zhu, Y. Li, F. Wang and H. He, *Chem. Eng. J.*, **155**, 83 (2009); https://doi.org/10.1016/j.cej.2009.06.039
22. K.S. Kumar, C.G. Song, G.M. Bak, G. Heo, M.J. Seong and J.W. Yoon, *J. Alloys Compd.*, **617**, 683 (2014); https://doi.org/10.1016/j.jallcom.2014.08.067
23. H. Zhang, K. Tan, H. Zheng, Y. Gu and W.F. Zhang, *Mater. Chem. Phys.*, **125**, 156 (2011); https://doi.org/10.1016/j.matchemphys.2010.08.087
24. B. Zhao, J. Wang, H. Li, Y. Xu, H. Yu, X. Jia, X. Zhang and Y. Hao, *ACS Sustain. Chem. Eng.*, **3**, 1518 (2015); https://doi.org/10.1021/acssuschemeng.5b00221
25. X. Qu, Y. Hou, M. Liu, L. Shi, M. Zhang, H. Song and F. Du, *Results Phys.*, **6**, 1051 (2016); https://doi.org/10.1016/j.rinp.2016.11.021
26. Y. Du, X. Zhang, Y. Shi, X. Hou, F. Li, Q. Zhang, Q. Tai, P. Liu and X.-Z. Zhao, *J. Alloys Compd.*, **890**, 161909 (2022); https://doi.org/10.1016/j.jallcom.2021.161909
27. A. Wang, H. Wang, S. Zhang, C. Mao, J. Song, H. Niu, B. Jin and Y. Tian, *Appl. Surf. Sci.*, **282**, 704 (2013); https://doi.org/10.1016/j.apsusc.2013.06.038
28. M. Li, Y. Huan, X. Yan, Z. Kang, Y. Guo, Y. Li, X. Liao, R. Zhang and Y. Zhang, *ChemSusChem*, **11**, 171 (2018); https://doi.org/10.1002/cssc.201701911
29. C. Zhang, L. Deng, P. Zhang, X. Ren, Y. Li and T. He, *Int. J. Electrochem. Sci.*, **12**, 4610 (2017); https://doi.org/10.20964/2017.05.100
30. P. O'brien, J.H. Park and J. Waters, *Thin Solid Films*, **431-432**, 502 (2003); https://doi.org/10.1016/S0040-6090(03)00244-X
31. A. Gahtar, C. Zaouche, A. Ammari and L. Dahbi, *Chalcogenide Lett.*, **20**, 377 (2023); https://doi.org/10.15251/CL.2023.205.377
32. K.S. Prasad, S. Prajapati and K. Selvaraj, *Korean J. Chem. Eng.*, **32**, 1986 (2015); https://doi.org/10.1007/s11814-015-0041-y
33. T. Li, K. Jiang, Y. Li, H. Luo, Z. Wang and Y.Q. Liu, *Int. J. Hydrogen Energy*, **48**, 7337 (2023); https://doi.org/10.1016/j.ijhydene.2022.11.107
34. Z. Wang, X. Liao, M. Zhou, F. Huang, K.A. Owusu, J. Li, Z. Lin, Q. Sun, X. Hong, C. Sun, Y. Cheng, Y. Zhao and L. Mai, *Energy Environ. Mater.*, **6**, e12409 (2023); https://doi.org/10.1002/eem2.12409
35. J. Wu, G. Xie, J. Lin, Z. Lan, M. Huang and Y. Huang, *J. Power Sources*, **195**, 6937 (2010); https://doi.org/10.1016/j.jpowsour.2010.04.081
36. H. Seema, Z. Zafar and A. Samreen, *Arab. J. Chem.*, **13**, 4978 (2020); https://doi.org/10.1016/j.arabjc.2020.01.020
37. L. Lin, S.A. Starostin, X. Ma, S. Li, S.A. Khan and V. Hessel, *React. Chem. Eng.*, **4**, 891 (2019); https://doi.org/10.1039/C8RE00357B
38. A.J. Abdulghani and W.M. Al-Ogedy, *Iraqi J. Sci.*, **56(2C)**, 1572 (2015).
39. Y. Zhang, S. Yuan, Y. Zhao, H. Wang and C. He, *J. Mater. Chem. A Mater. Energy Sustain.*, **2**, 7897 (2014); https://doi.org/10.1039/C4TA01057D
40. G. Jerkiewicz, *ACS Catal.*, **12**, 2661 (2022); https://doi.org/10.1021/acscatal.1c06040
41. A.K. Swarnkar, S. Sahare, N. Chander, R.K. Gangwar, S.V. Bhoraskar and T.M. Bhave, *J. Exp. Nanosci.*, **10**, 1001 (2015); https://doi.org/10.1080/17458080.2014.951410
42. A.K. Reddy, M. Gurulakshmi, K. Susmitha, M. Raghavender, N. Thota and Y.V. Subbaiah, *J. Mater. Sci. Mater. Electron.*, **31**, 4752 (2020); https://doi.org/10.1007/s10854-020-03032-3
43. P. Baskaran, K.D. Nisha, S. Harish, S. Prabakaran, M. Navaneethan, J. Archana, S. Ponnusamy, C. Muthamizhchelvan and H. Ikeda, *J. Mater. Sci.*, **56**, 4135 (2021); https://doi.org/10.1007/s10853-020-05421-9
44. V.D. Dao, D.V. Quang, N.H. Vu, H.H.T. Vu, N.D. Hoa, V.T. Duoc, N.V. Hieu, T.H. Nguyen and N.A. Tran, *Vietnam J. Chem.*, **57**, 784 (2019); https://doi.org/10.1002/vjch.2019000114
45. T. Shanmugapriya and J. Balavijayalakshmi, *J. Cluster Sci.*, **32**, 1277 (2021); https://doi.org/10.1007/s10876-020-01890-9
46. E. Emil and S. Gürmen, *Mater. Sci. Technol.*, **34**, 1549 (2018); https://doi.org/10.1080/02670836.2018.1490857
47. P.C. Nagajyothi, M. Pandurangan, M. Veerappan, D.H. Kim, T.V.M. Sreekanth and J. Shim, *Mater. Lett.*, **216**, 58 (2018); https://doi.org/10.1016/j.matlet.2017.12.081
48. M. Indhumathy and A. Prakasam, *J. Cluster Sci.*, **31**, 91 (2020); https://doi.org/10.1007/s10876-019-01620-w
49. T. Fazal, S. Iqbal, M. Shah, B. Ismail, N. Shaheen, H. Alrbyawi, M.M. Al-Anazy, E.B. Elkaeed, H.H. Somaily, R.A. Pashameah, E. Alzahrani and A.-E.A. Farouk, *Molecules*, **27**, 6419 (2022); https://doi.org/10.3390/molecules27196419
50. M. Kamalanathan, S. Karuppusamy, R. Sivakumar and R. Gopalakrishnan, *J. Mater. Sci.*, **50**, 8029 (2015); https://doi.org/10.1007/s10853-015-9370-9
51. B. Noorani, S. Ghasemi and S.R. Hosseini, *J. Photochem. Photobiol. Chem.*, **405**, 112966 (2021); https://doi.org/10.1016/j.jphotochem.2020.112966
52. C.A. Pandey, S. Ravuri, R. Ramachandran, R. Santhosh, S. Ghosh, S.R. Sitaraman and A.N. Grace, *Int. J. Nanosci.*, **17**, 1760021 (2018); https://doi.org/10.1142/S0219581X17600213